RSC Advances

PAPER

View Article Online
View Journal | View Issue

Cite this: *RSC Adv.*, 2016, **6**, 24115

Graphene quantum dots-decorated ZnS nanobelts with highly efficient photocatalytic performances†

Sooho Ham, Yeonho Kim,‡ Myung Jin Park, Byung Hee Hong and Du-Jeon Jang*

Received 30th December 2015
Accepted 25th February 2016

DOI: 10.1039/c5ra28026e

www.rsc.org/advances

Hybrid nanostructures combining inorganic materials and graphene have shown great potential for the environmentally friendly treatment of effluents. Herein, graphene quantum dots (GQDs)-decorated ZnS nanobelts have been synthesized *via* a facile hydrothermal method. The electrostatic attraction of two materials and the thermal reduction of graphene are the main driving forces to fabricate well-defined composite nanostructures. GQDs in GQD/ZnS nanocomposites have been found to exist discretely and uniformly on the surfaces of ZnS nanobelts. The photocatalytic activity of GQD/ZnS nanocomposites has been found to be highest at a GQD/ZnS mass ratio of 8×10^{-4}. The photocatalytic rate constant (0.0046 min^{-1}) of GQD/ZnS nanocomposites having the optimized GQD content in the photodegradation reaction of rhodamine B has been found to be 14 times higher than that of commercially available ZnS powder. Decorated GQDs introduce an additional visible-light response and serve as electron collectors and transporters to block electron–hole recombination efficiently, enhancing the photocatalytic performances of ZnS nanobelts immensely.

Introduction

The design and controlled fabrication of nanostructured materials having functional properties have been extensively studied.[1–6] With growing concern over environmental remediation and energy conversion, nanoscaled semiconductors have gained considerable interest in photocatalysis,[7–11] especially in the decomposition of organic water pollutants such as colored dyes into CO_2 and H_2O using solar light.[12–16] In particular, metal sulfides have attracted significant attention in photocatalysis due to their suitable band gap and catalytic function.[15,16] Among them, zinc sulfide (ZnS), a kind of nontoxic and abundant chalcogenide materials, with direct band gaps (3.72 eV and 3.77 eV for cubic zinc blende and hexagonal wurtzite, respectively) is a promising candidate for photocatalysts in environmental remediation[16–19] owing to its unique properties: the rapid generation of electron–hole pairs by photoexcitation and the highly negative reduction potential of its conduction band.[20] However, the fast recombination rate of photogenerated electron–hole pairs and the narrow absorption bands of its nanostructures restrict its practical applications as photocatalysts.[21,22] To overcome these issues, ZnS photocatalysts have been modified chemically in combination with noble metals, different semiconductors, or carbonaceous materials.[23–25] It has been demonstrated that heterostructures often exhibit superior properties or new features compared with their individual constituents, due to coupling effects that can induce significant enhancement in the generation, transportation, and prolonged lifetime of charge carriers.[26–28]

Graphene quantum dots (GQDs) have received much attention because they are non-toxic, inexpensive, free of heavy metals, and environmentally friendly, compared with traditional quantum dots based on toxic heavy metals which can cause serious health and environmental issues. GQDs are useful for photocatalysis applications owing to their photoinduced electron-transfer properties.[30,31] Moreover, the good dispersity of GQDs in common solvents is expected to enable various solution-processable applications.[32] Thus, the combination of ZnS and GQDs seems to be an ideal means of improving charge separation by hindering charge recombination, thus enhancing photocatalytic efficiency.

Herein, we present the fabrication of GQDs-decorated ZnS (G/ZnS) nanobelts with varied mass ratios of GQD/ZnS from 1×10^{-4} to 2×10^{-3} *via* a facile hydrothermal process. ZnS nanobelts have been decorated with GQDs *via* a spontaneous close-contact process through electrostatic attraction to the surface of ZnS nanobelts and a subsequent tight-binding process through the thermal reduction of GQDs onto ZnS nanobelts.[41] The band-gap energies of G/ZnS nanocomposites have been estimated to be smaller than those of pristine ZnS nanobelts. As-prepared G/ZnS photocatalysts have been found to photocatalyze the degradation of rhodamine B with remarkably enhanced efficiency in comparison with individual constituents due to the effective separation of photoinduced electron–hole pairs (Fig. 1).

Department of Chemistry, Seoul National University, Seoul 08826, Korea. E-mail: djjang@snu.ac.kr

† Electronic supplementary information (ESI) available. See DOI: 10.1039/c5ra28026e

‡ Present address: Nano-Bio Electron Microscopy Research Group, Korea Basic Science Institute, Daejeon 34133, Korea.

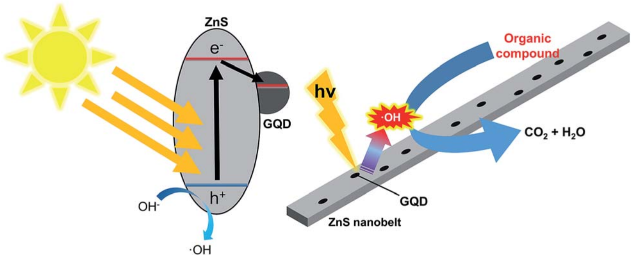

Fig. 1 Schematic for a plausible decomposition mechanism of an organic dye over a G/ZnS nanocomposite under light irradiation.

Experimental

Synthesis of ZnS nanobelts

Single-crystalline wurtzite ZnS nanobelts were prepared *via* a reported wet-chemical solution process.[6]

Fabrication of GQDs

Carbon fibers (300 mg, purchased from Fibre Glast Development Corporation) were added into a mixture containing 60 mL of 18 M H_2SO_4(aq) and 20 mL of 16 M HNO_3(aq). The mixed solution was stirred at 80 °C for 24 h, cooled down to room temperature, and diluted with water (800 mL). The diluted solution was dialyzed in a dialysis bag retaining molecular weight of 1000 Da for 3 days to remove the acids.

Fabrication of GQDs–ZnS nanocomposites

20 mg of as-prepared ZnS nanobelts was dispersed in 30 mL water and ultrasonicated for 10 min. Subsequently, a calculated specific volume of 0.1 mg mL^{-1} GQD in water was dropped slowly into the ZnS containing solution. GQD/ZnS mass ratios were varied from 1×10^{-4} to 2×10^{-3}; if the 10^3-multiplied weight ratio of GQDs to ZnS nanobelts was *x*, the nanocomposite sample of GQDs-decorated ZnS nanobelts was designated as *x* G/ZnS. The mixture solution was then loaded into a Teflon-lined stainless-steel autoclave of 50 mL capacity, placed in a preheated oven at 180 °C for 6 h, and cooled to room temperature. The color of produced G/ZnS nanocomposites was found to be grayish-white. The precipitated product was repeatedly centrifuged and washed with ethanol and water, and dried in a vacuum at 60 °C for 6 h to yield the final powder product of G/ZnS nanocomposites.

Characterization

High-resolution transmission electron microscopic (HRTEM) images and energy-dispersive X-ray (EDX) elemental mappings were recorded using a JEOL JEM-2100F high-resolution microscope. X-ray diffraction (XRD) patterns were obtained with a Bruker D8 DISCOVER diffractometer using Cu K_α radiation (0.15418 nm). X-ray photoelectron spectroscopy (XPS) spectra were collected with a Thermo Scientific Sigma Probe ESCA spectrometer using an X-ray source of Al K_α, and the measured binding energies were calibrated with the C 1s peak at 284.5 eV of contaminated carbon. While Fourier transform infrared (FTIR) spectra were obtained using a Thermo Scientific Nicolet 6700 spectrometer, extinction spectra were measured using a Scinco S3100 UV-vis spectrophotometer. Photoluminescence spectra were measured using a JASCO FP-8300 spectrofluorometer, and surface charges were measured using a Malvern instruments Nano ZS90 zetasizer.

Photocatalytic experiments

The evaluation of the photocatalytic performances of as-prepared samples was performed at ambient conditions with rhodamine B (RhB) as a representative dye. In a typical procedure, 5 mg of a G/ZnS catalyst was added to 40 mL of 10 μM RhB(aq) and stirred in the dark for 30 min to ensure the adsorption–desorption equilibrium of RhB on the nanocatalyst surface. The reaction mixture was placed 30 cm away from a 300 W Schoeffel LPS 255 HR xenon arc lamp, and its aliquots were taken at scheduled intervals during irradiation and centrifuged to separate the supernatant, whose UV/vis absorption spectrum was then recorded to monitor the concentration of remnant RhB.

Results and discussion

Structural characteristics

All the diffraction peaks of both 0.8 G/ZnS nanocomposites and pristine ZnS nanobelts in Fig. 2 can be indexed as the reference peaks of wurtzite ZnS (JCPDS card no. 36-1450). The absence of the typical stacking peak at 26° indicates that the added amount of GQDs (a GQD/ZnS mass ratio of 8×10^{-4}) was too small to show any new diffraction peaks from stacking or conglomeration of GQDs during thermal reduction.[43] None of the XRD peaks have been attributed to impurity, suggesting that our as-prepared G/ZnS nanocomposites maintain the high structural purity of wurtzite ZnS. The inset of Fig. 2 displays that the diffraction peaks of 0.8 G/ZnS nanocomposites are broader to some extent than the respective ones of pristine ZnS nanobelts, indicating that the mean crystal diameter of ZnS nanobelts has been decreased slightly during hybridization with GQDs. The mean crystallite diameters of ZnS nanobelts and 0.8 G/ZnS nanocomposites, estimated from the line widths of the peaks at the 2θ value of 27° using the Scherrer's formula,[29] have been

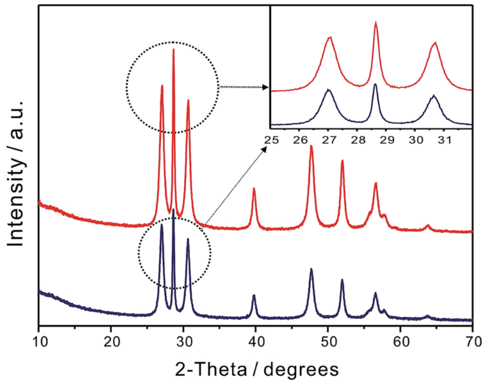

Fig. 2 XRD patterns of 0.8 G/ZnS nanocomposites (red) and pristine ZnS nanobelts (blue).

found to be 12.5 and 11.5 nm, respectively, meaning that the mean crystal size of ZnS nanobelts has been decreased due to surface decoration with GQDs.

HRTEM images and EDX elemental maps

The HRTEM image of Fig. 3A clearly shows that GQDs with an average diameter of 20 nm have been decorated successfully onto ZnS nanobelts *via* a hydrothermal process. Although the morphology and structure of ZnS nanobelts have been maintained during the hybridization process, the average size of GQDs has been increased due to aggregation. The initial average diameter of synthesized GQDs has been estimated as about 5 nm from the HRTEM image of Fig. S1.† During the hydrothermal treatment, GQDs have been reduced to decrease the surface charge of GQDs, thus alleviating electrostatic repulsion between GQDs. Eventually GQDs have been found to form aggregates, and the apparently observed average size of GQDs has been increased. The HRTEM image of Fig. 3B reveals that interplanar spacings of 0.29, 0.31, and 0.33 nm agree very well with the respective standard separations of the (101), the (002), and the (100) planes of wurtzite ZnS.[6,29] Hexagonal atomic lattice with uniform contrast, originating from monolayer graphene, can be also clearly discerned in the enlarged HRTEM view of Fig. 3B.[33,42] The distribution maps of the constituting elements, Zn, S, and C in the panels D, E, and F of Fig. 3, respectively, demonstrate that ZnS have been decorated with GQDs. Furthermore, Fig. 3F indicates that GQDs in 0.8 G/ZnS nanocomposites with a GQD/ZnS mass ratio of 8 × 10^{-4} exist discretely and uniformly on the surfaces of ZnS nanobelts.

Surface properties

To confirm electrostatic attraction between ZnS nanobelts and GQDs, the surface charges have been measured. Before the hydrothermal reduction, the surface charges of ZnS nanobelts and GQDs were +10 meV and −30 meV, respectively, thus, suggesting that ZnS nanobelts and GQDs are close-contacted *via* electrostatic attraction. To understand the binding states of the constituent elements of GQDs-decorated ZnS nanobelts, we have measured the XPS spectra of 0.8 G/ZnS nanocomposites (Fig. 4). The peak energies of 1021.6 and 1044.7 eV in Fig. 4A have been identified as the binding energies of the Zn $2p_{3/2}$ and $2p_{1/2}$ of ZnS, respectively. The XPS spectrum of Fig. 4B has been deconvoluted into two Gaussian bands, whose peak energies of 160.9 and 162.1 eV have been assigned to the binding energies of the S $2p_{3/2}$ and $2p_{1/2}$ of ZnS, respectively.[34] The XPS spectrum of C 1s (Fig. 4C) has been deconvoluted into three Gaussian bands located at 284.5,

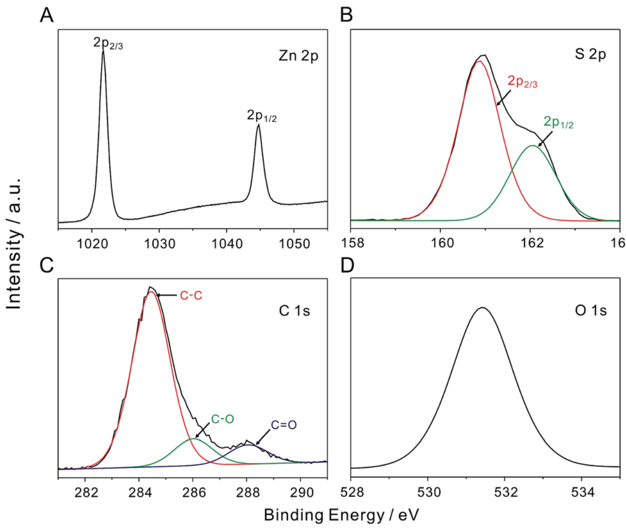

Fig. 4 Zn 2p (A), S 2p (B), C 1s (C), and O 1s (D) XPS spectra of 0.8 G/ZnS nanocomposites. The S 2p and C 1s spectra have been deconvoluted into two and three Gaussian curves, respectively.

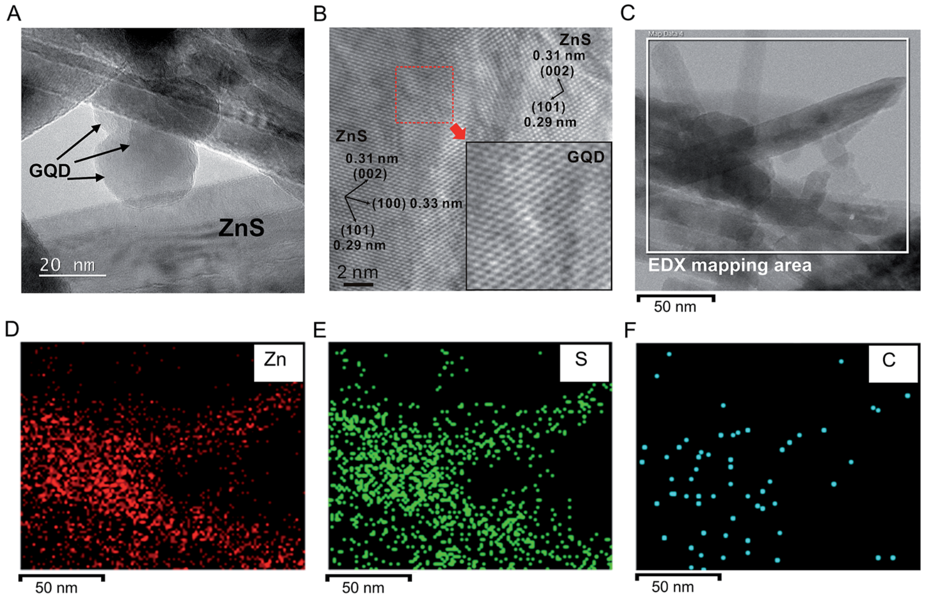

Fig. 3 HRTEM images (A–C) and the elemental maps of Zn, S, and C (D–F) of 0.8 G/ZnS nanocomposites.

286.0, and 288.1 eV, which can be ascribed to C–C bonds, C–O bonds, and C═O bonds, respectively. Compared to the C 1s XPS spectrum of pristine GQDs (Fig. S2†), the relative intensity of C–O bonds has decreased after the hydrothermal treatment, meaning that the thermal treatment has reduced GQDs by decomposing C–O and C–OH groups to form stable bonds between ZnS nanobelts and GQDs. However, Fig. 4D shows that only one XPS peak at 531.4 eV can be attributed to O 1s, probably because the binding energy of O 1s in the surface hydroxyl bonds of graphene[35–37] is similar to that of O 1s in C═O bonds (see below); note that the band widths (1.95 eV) of O 1s in Fig. 4D is substantially broader than that (1.68 eV) of the C 1s of C–C bonds in Fig. 4C. Nevertheless, our XPS results also support that GQDs have been successfully incorporated with ZnS nanobelts to form G/ZnS nanocomposites.

Based on the discussion of the XPS analysis, there are different carbon functional groups on the surface of 0.8 G/ZnS nanocomposites, which can also be seen in the FTIR spectrum of Fig. 5. The broad absorption band located around 3250 cm^{-1} can be assigned to the stretching vibration of O–H, while the characteristic lines at 2940 and 1718 cm^{-1} correspond to the asymmetric stretching of $-\mathrm{CH}_2$ and the stretching vibration of C═O, respectively.[38,39] The absorption peaks at 1601 and 1413 cm^{-1} have been attributed to the stretching vibration of C═C and the O–H deformation of C–OH, respectively, and the absorption peaks at 1261 and 1060 cm^{-1} have been assigned to the stretching vibrational modes of C–OH and C–OC, respectively.[39,40] Consequently, not only the XPS spectra of Fig. 4 but also the FTIR spectrum of Fig. 5 support that GQDs have been decorated to ZnS nanobelts with maintaining the inherent characteristics of graphene oxide and graphene.

Optical properties

The extinction spectra of Fig. 6A show that both samples of 0.8 G/ZnS nanocomposites and 0.0 G/ZnS nanobelts have the representative band-gap absorption of ZnS nanobelts in the ultraviolet region. The enhanced absorption of 0.8 G/ZnS nanocomposites in the entire visible region can be attributed to the presence of graphene. However, in comparison with the extinction spectrum of 0.0 G/ZnS nanobelts, that of G/ZnS nanocomposites shows the obvious red shift of the absorption edge by 14 nm due to the chemical interactions of ZnS with graphene. It is well known that ZnS is a direct semiconductor, whose band gap can be estimated by extrapolating the linear portion of the modified Kubelka–Munk function[29] *versus* the energy of light (Fig. 6B). The derived band gaps of 0.0 G/ZnS and 0.8 G/ZnS nanocomposites have been estimated as 3.69 and 3.40 eV, respectively, indicating that coupling with graphene narrows the band gap of semiconductor ZnS in G/ZnS nanocomposites. We suggest that band-gap narrowing as well as increased visible-light absorption due to graphene decoration enhances the photocatalytic performances of G/ZnS nanocomposites (see below).

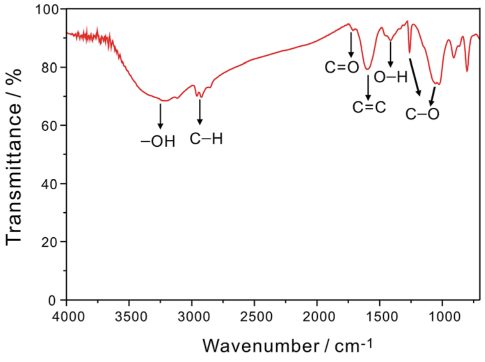

Fig. 5 FTIR spectrum of 0.8 G/ZnS nanocomposites.

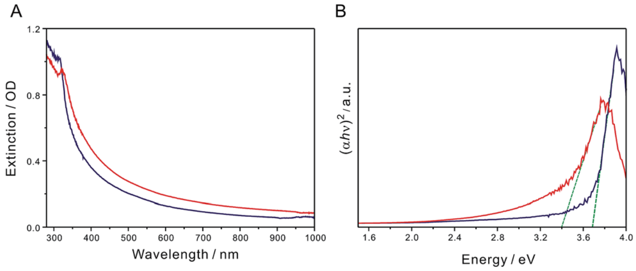

Fig. 6 Extinction spectra (A) and Kubelka–Munk plots (B) of 0.8 G/ZnS nanocomposites (red) and 0.0 G/ZnS nanobelts (blue) suspended in ethanol. The green solid lines in panel B show the best linear fits to estimate the band-gap energy.

Photocatalytic activities

The photocatalytic degradation of RhB under light irradiation at ambient conditions has been monitored to evaluate the photocatalytic activities of G/ZnS nanocatalysts. Fig. 7A indicates that the concentration of RhB under light irradiation was decreased most rapidly under the photocatalysis of 0.8 G/ZnS nanocomposites while that was hardly reduced in the absence of any catalysts. The $\ln(C/C_0)$-*vs.*-t kinetic plots of the photocatalytic degradation of RhB under light irradiation in the presence of G/ZnS nanocomposites have been also given in Fig. 7B; the photodegradation kinetic plots of RhB *via* G/ZnS nanocomposites follow pseudo first-order kinetics. Fig. 7C shows that the photocatalytic activity of G/ZnS nanocomposites in the photodegradation reaction of RhB was increased with the increase of the GQD/ZnS mass ratio until the ratio became 8×10^{-4}. This indicates indeed that hybridization with graphene enhances the photocatalytic activity of ZnS nanoparticles immensely. However, the photocatalytic activity decreases with the concentration increase of GQDs above the GQD/ZnS mass ratio of 8×10^{-4}. We consider that excessive GQDs can act as charge-recombination centers instead of electron pathways. Table 1 reveals that the observed photocatalytic rate constant of 0.8 G/ZnS nanocomposites (0.046 min^{-1}) is 14 times higher than that of commercially available ZnS powder (99.99%, 10 μm, purchased from Sigma-Aldrich) and 1.9 times higher than that of 0.0 G/ZnS. As photocorrosion is a major concern for sulfide semiconductors, the stability of as-formed G/ZnS nanocomposites has been tested *via* photocatalyst recycling

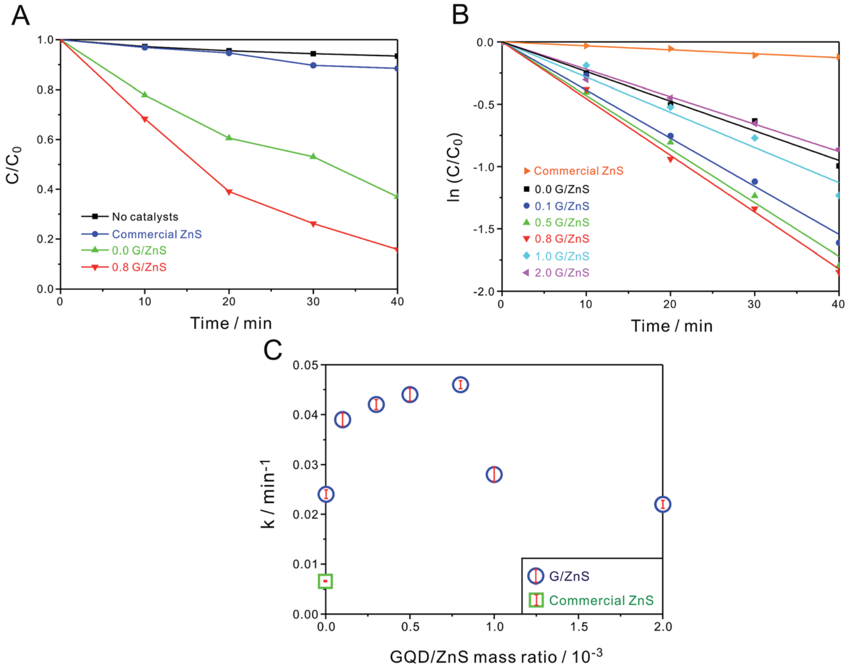

Fig. 7 Concentration changes (A), first-order kinetic profiles (B), and decay rate constants (C) of RhB *via* indicated photocatalysts.

tests (Fig. S3†). 70% of the photocatalytic degradation efficiency has remained after two recycling experiments.

The photocatalytic mechanism of G/ZnS nanocomposites can be suggested as follows: photogenerated holes from ZnS nanobelts can react with OH^- ions to form $^\bullet OH$ radicals for the further photocatalytic degradation of RhB (Fig. 1). During the photocatalytic process, GQDs serve as electron collectors and transporters to block electron–hole recombination efficiently, generating long-lived holes on the surfaces of ZnS nanobelts. The photoluminescence spectra have been measured to test the electron–hole recombination of G/ZnS nanocomposites (Fig. S4†). The band-edge emission of ZnS nanobelts around 324 nm has been drastically quenched by presence of GQDs, supporting that the electron–hole pairs of ZnS nanobelts have been separated extensively *via* the effective transfer of excited electrons to GQDs. Longer-lived holes then account for the largely enhanced photocatalytic activity of G/ZnS nanocomposites. The thermal reduction of GQDs onto the ZnS nanobelts directly without having any linker molecules brings about new visible absorption to our G/ZnS nanocomposites; newly generated electrons in the Fermi level of graphene with leaving holes to the valence-band level of ZnS induce band-gap narrowing to G/ZnS nanocomposites. Because the Fermi level of ZnS is lower than that of graphene and GQDs attached to ZnS nanobelts, the energy band of G/ZnS nanocomposites will curve up to form a metal–semiconductor Schottky junction under equilibrium. The excited electrons of graphene are not allowed to transfer to the conduction band of ZnS due to the energy barrier between graphene and ZnS. This energy barrier also facilitates charge-separation processes and effectively reduces recombination chances of newly generated electrons and holes, significantly increasing the lifetime of charges in G/ZnS nanocomposites. Long-lived charges are then suggested to enhance the photocatalytic performances of G/ZnS nanocomposites on a large scale.

Table 1 Catalytic degradation rate constant of RhB *via* nanocatalysts under irradiation of a 300 W Xe lamp

Nanocatalyst	GQD/ZnS mass ratio (10^{-3})	k ($\min^{-1}$)
No catalysts	—	0.002
Commercial ZnS	0.0	0.003
0.0 G/ZnS	0.0	0.024
0.1 G/ZnS	0.1	0.039
0.2 G/ZnS	0.2	0.042
0.5 G/ZnS	0.5	0.043
0.8 G/ZnS	0.8	0.046
1.0 G/ZnS	1.0	0.028
2.0 G/ZnS	2.0	0.022

Conclusions

Highly efficient photocatalysts of GQDs-decorated ZnS nanobelts have been developed *via* a facile hydrothermal process. The decoration of ZnS nanobelts with GQDs has been carried out *via* two synthetic steps: the spontaneous attachment of GQDs on the surface of ZnS nanobelts through electrostatic attraction, followed by the partial thermal reduction of GQDs to construct well-defined composite nanostructures. Measurements of XRD, HRTEM, XPS, and FTIR have revealed that GQDs in G/ZnS nanocomposites exist discretely and uniformly on the surfaces of ZnS nanobelts. It has been found that decorated GQDs introduce additional visible-light response and serve as electron collectors and transporters to block electron–hole recombination efficiently, enhancing the photocatalytic activity of ZnS nanobelts extensively. The photocatalytic activity of G/ZnS nanocomposites has been found to be highest at a GQD/ZnS mass ratio of 8×10^{-4}. The photocatalytic rate constant of 0.8 G/ZnS nanocomposites (0.0046 min^{-1}) in the photodegradation reaction of RhB has been found to be 14 times higher than that of commercially available ZnS powder.

Acknowledgements

This work was supported by research grants through the National Research Foundation of Korea funded by the Korean government (2014-057382 and 2015-051798).

References

1 D. Choi, J.-Y. Pyo, Y. Kim and D.-J. Jang, *J. Mater. Chem. C*, 2015, **3**, 3286–3293.
2 A. Iwase, Y. H. Ng, Y. Ishiguro, A. Kudo and R. Amal, *J. Am. Chem. Soc.*, 2011, **133**, 11054–11057.
3 H.-H. Li, S.-Y. Ma, Q.-Q. Fu, X.-J. Liu, L. Wu and S.-H. Yu, *J. Am. Chem. Soc.*, 2015, **137**, 7862–7868.
4 Y. Kim and D.-J. Jang, *Chem. Commun.*, 2013, **49**, 8940–8942.
5 A. Hernández-Gordillo, M. Arroyo, R. Zanella and V. Rodríguez-González, *J. Hazard. Mater.*, 2014, **268**, 84–91.
6 Y. Kim, S. J. Kim, S.-P. Cho, B. H. Hong and D.-J. Jang, *Sci. Rep.*, 2015, **5**, 12345.
7 X. Xu, C. Randorn, P. Efstathiou and J. T. Irvine, *Nat. Mater.*, 2012, **11**, 595–598.
8 A. Kudo and Y. Miseki, *Chem. Soc. Rev.*, 2009, **38**, 253–278.
9 H.-B. Kim, H. Kim, W. I. Lee and D.-J. Jang, *J. Mater. Chem. A*, 2015, **3**, 9714–9721.
10 A. Hernández-Gordillo, A. G. Romero, F. Tzompantzi and R. Gómez, *Appl. Catal., B*, 2014, **144**, 507–513.
11 S. J. Moniz, S. A. Shevlin, D. J. Martin, Z.-X. Guo and J. Tang, *Energy Environ. Sci.*, 2015, **8**, 731–759.
12 R. Asahi, T. Morikawa, T. Ohwaki, K. Aoki and Y. Taga, *Science*, 2001, **293**, 269–271.
13 L. Zhang, L. Du, X. Yu, S. Tan, X. Cai, P. Yang, Y. Gu and W. Mai, *ACS Appl. Mater. Interfaces*, 2014, **6**, 3623–3629.
14 A. Gupta, K. Mondal, A. Sharma and S. Bhattacharya, *RSC Adv.*, 2015, **5**, 45897–45907.
15 Y. Kim, H.-B. Kim and D.-J. Jang, *J. Mater. Chem. A*, 2014, **2**, 5791–5799.
16 D. Chen, F. Huang, G. Ren, D. Li, M. Zheng, Y. Wang and Z. Lin, *Nanoscale*, 2010, **2**, 2062–2064.
17 M. Muruganandham and Y. Kusumoto, *J. Phys. Chem. C*, 2009, **113**, 16144–16150.
18 M. Sharma, T. Jain, S. Singh and O. Pandey, *Sol. Energy*, 2012, **86**, 626–633.
19 S. Xiong, B. Xi, C. Wang, D. Xu, X. Feng, Z. Zhu and Y. Qian, *Adv. Funct. Mater.*, 2007, **17**, 2728–2738.
20 H. Yin, Y. Wada, T. Kitamura and S. Yanagida, *Environ. Sci. Technol.*, 2001, **35**, 227–231.
21 D. F. Moore, Y. Ding and Z. L. Wang, *J. Am. Chem. Soc.*, 2004, **126**, 14372–14373.
22 T. Luttrell, S. Halpegamage, J. Tao, A. Kramer, E. Sutter and M. Batzill, *Sci. Rep.*, 2014, **4**, 4043.
23 J. Zhang, Y. Wang, J. Zhang, Z. Lin, F. Huang and J. Yu, *ACS Appl. Mater. Interfaces*, 2013, **5**, 1031–1037.
24 E. Hong, D. Kim and J. H. Kim, *J. Ind. Eng. Chem.*, 2014, **20**, 3869–3874.
25 Y. Zhang, N. Zhang, Z.-R. Tang and Y.-J. Xu, *ACS Nano*, 2012, **6**, 9777–9789.
26 Y. Tang, X. Liu, C. Ma, M. Zhou, P. Hou, L. Yu, J. Pan, W. Shi and Y. Yan, *New J. Chem.*, 2015, **39**, 5150–5160.
27 Y. Zheng, L. Zheng, Y. Zhan, X. Lin, Q. Zheng and K. Wei, *Inorg. Chem.*, 2007, **46**, 6980–6986.
28 J. Wang, Y. Li, J. Ge, B.-P. Zhang and W. Wan, *Phys. Chem. Chem. Phys.*, 2015, **17**, 18645–18652.
29 Y. Kim and D.-J. Jang, *RSC Adv.*, 2013, **3**, 16945–16948.
30 D. Qu, M. Zheng, P. Du, Y. Zhou, L. Zhang, D. Li, H. Tan, Z. Zhao, Z. Xie and Z. Sun, *Nanoscale*, 2013, **5**, 12272–12277.
31 S. Zhuo, M. Shao and S.-T. Lee, *ACS Nano*, 2012, **6**, 1059–1064.
32 X. Wang, W. Tian, M. Liao, Y. Bando and D. Golberg, *Chem. Soc. Rev.*, 2014, **43**, 1400–1422.
33 D. I. Son, B. W. Kwon, D. H. Park, W.-S. Seo, Y. Yi, B. Angadi, C.-L. Lee and W. K. Choi, *Nat. Nanotechnol.*, 2012, **7**, 465–471.
34 G. Wang, B. Huang, Z. Li, Z. Lou, Z. Wang, Y. Dai and M.-H. Whangbo, *Sci. Rep.*, 2015, **5**, 8544.
35 S. Some, Y. Kim, Y. Yoon, H. Yoo, S. Lee, Y. Park and H. Lee, *Sci. Rep.*, 2013, **3**, 1929.
36 N. Han, T. V. Cuong, M. Han, B. D. Ryu, S. Chandramohan, J. B. Park, J. H. Kang, Y.-J. Park, K. B. Ko, H. Y. Kim, H. K. Kim, J. H. Ryu, Y. Katharria, C.-J. Choi and C.-H. Hong, *Nat. Commun.*, 2013, **4**, 1452.
37 L. Wang, Y. Wang, T. Xu, H. Liao, C. Yao, Y. Liu, Z. Li, Z. Chen, D. Pan, L. Sun and M. Wu, *Nat. Commun.*, 2014, **5**, 5357.
38 H. Zhang, D. Hines and D. L. Akins, *Dalton Trans.*, 2014, **43**, 2670–2675.
39 V. H. Pham, T. V. Cuong, S. H. Hur, E. Oh, E. J. Kim, E. W. Shin and J. S. Chung, *J. Mater. Chem.*, 2011, **21**, 3371–3377.
40 N. Kumar, S. Das, C. Bernhard and G. D. Varma, *Supercond. Sci. Technol.*, 2013, **26**, 095008.
41 Y. Zhou, Q. Bao, L. A. L. Tang, Y. Zhong and K. P. Loh, *Chem. Mater.*, 2009, **21**, 2950–2956.
42 J. K. Kim, M. J. Park, S. J. Kim, D. H. Wang, S. P. Cho, S. Bae, J. H. Park and B. H. Hong, *ACS Nano*, 2013, **7**, 7207–7212.
43 J. Ryu, E. Lee, S. Lee and J. Jang, *Chem. Commun.*, 2014, **50**, 15616–15618.